Engineering and Technology Journal
Journal homepage: https://etj.uotechnology.edu.iq

Performance and exergoeconomic assessment of of integrated organic rankine cycle with solar combined cycle system on sustainable power generation in Iraq

Abdulrazzak Akroot*, Ayaa Faraj

Mechanical Engineering Dept, Faculty of Engineering, Karabük University, 78050, Karabük, Turkey.
*Corresponding author Email: abdulrazzakakkroot@karabuk.edu.tr

HIGHLIGHTS

- A solar triple cycle with PTCs, TES, and Brayton-Rankine-ORC improves efficiency and ensures continuous power
- Seasonal changes affect performance; March yields 42.55 MW, while July has the lowest output and highest cost
- Exergy destruction totals were 82.255 MW, with PTC losses at 66.93 MW and peak costs reaching $906.52 per hour
- System optimization raises gas turbine inlet temperature and adjusts RC boiler pinch point to reduce costs

Keywords:
Triple Combined Cycle (TCC)
Solar power
Exergoeconomic analysis
Rock bed storage system
Iraq

ABSTRACT

This study presents a comprehensive performance and exergoeconomic assessment of a solar-driven triple combined cycle (TCC) power system integrated with a rock bed thermal storage unit and an Organic Rankine Cycle (ORC) for enhanced sustainable power generation in Iraq. The proposed system combines Brayton, Rankine, and Organic Rankine Cycle (ORC) cycles to maximize energy recovery from both high- and low-grade heat sources. The integration of the ORC unit significantly improves system efficiency by utilizing residual thermal energy that would otherwise be wasted. The analysis used Engineering Equation Solver (EES) software, incorporating monthly climatic data from Salahaddin, Iraq. Thermodynamic and exergoeconomic evaluations assessed energy efficiency, exergy destruction, component costs, and electricity production cost. Unlike previous studies, this research introduces an advanced exergoeconomic perspective, providing a more realistic assessment of technical and economic performance. Results indicate that the system achieves a power output of 12.4 MW in June, with energy and exergy efficiencies of 37.37% and 40.8%, respectively, and a unit electricity cost of $33.31 per hour. In January, the output increases to 14.17 MW with higher exergy efficiency (46.21%) but at a higher cost due to reduced solar availability. The addition of the ORC unit enhances both energy recovery and economic performance, especially during periods of low solar input, supporting the system's viability for year-round renewable power generation.

1. Introduction

Solar thermal power plants with thermal energy storage (TES) provide a practical alternative to traditional fossil fuel-based power generation [1]. Unlike traditional power plants, which rely on limited fossil fuel supplies and contribute to environmental degradation, solar thermal power plants use the sun's abundant energy to generate electricity without polluting the environment. These alternative energy systems are crucial in addressing climate change by reducing greenhouse gas emissions through the sustainable conversion of energy. It is advisable to integrate them with thermal energy storage (TES) systems to enhance their reliability, allowing for continuous energy production even during times of low solar radiation [2,3]. This approach optimizes solar energy utilization and ensures a stable electricity supply, improving system efficiency and grid integration [4].

A wide range of studies have investigated TES technologies and their application within power plant systems. Marongiu et al. [5], developed a 2D numerical model for a 450 kWhth rock bed storage unit, accounting for the temperature-dependent properties of air and rock. They analyzed the impact of airflow rate, rock size, rock type, and insulation on charge efficiency and heat loss. Soprani et al. [6], investigated and studied a lab-scale high-temperature thermal energy storage (HTTES) system using diabase rocks and air, designed to store heat at 600 °C with a capacity of 450 kWhth. They tested charging and discharging under various conditions, assessed flow behavior, and evaluated temperature profiles, as well as key performance metrics such as efficiency and losses. Muhammed et al. [7], developed and validated a 2-D model for a 1 MWh vertical-flow rock-based thermal storage unit using experimental data. They examined key design parameters affecting temperature distribution and charging

http://doi.org/10.30684/etj.2025.158167.1913
Received 12 March 2025; Received in revised form 29 May 2025; Accepted 06 June 2025; Available online 22 July 2025
2412-0758/University of Technology-Iraq, Baghdad, Iraq

efficiency. Desai et al. [8], proposed a cost-effective CSP system using a micro-structured polymer foil concentrator. They conducted a techno-economic analysis of three TES options: two-tank indirect, two-tank direct, and packed-bed rock thermocline, integrated with an ORC and MED unit for simultaneous power and water production. Zanganeh et al. [9], developed and tested a 6.5 MWhth rock-based thermal storage system using air as the heat transfer fluid. The unit, buried and shaped as a truncated cone, was designed to reduce heat loss and pressure drop. Fernández et al. [10], examined the thermal efficiency of packed-bed TES systems as cost-effective solutions for high-temperature heat storage. They evaluated three operational strategies — full charge/discharge, time restriction, and outlet temperature control — to analyze their impact on cycle efficiency, material utilization, and thermocline stability. Nahhas et al. [11], examined basalt rocks for thermal energy storage, evaluating properties such as thermal expansion, density, specific heat, and Young's modulus across various temperatures. The study identified 700 °C as a suitable operating limit, highlighting basalt's strong thermal capacity, conductivity, shock resistance, and environmental benefits. Öztürk et al. [12], proposed a hybrid system integrating a gas turbine, steam turbine, central receiver CSP plant, and rock bed thermal storage to generate power and supply heat for drying and district heating. The study performed detailed energy and exergy analyses to evaluate system efficiency and irreversibilities under varying conditions. Heller and Gauche [13], developed a heat transfer model for a rock-packed bed designed to store thermal energy from a solar receiver or fossil combustor and supply it to a steam cycle in a combined-cycle CSP plant. Sharma et al. [14], investigated the charging and discharging performance of packed-bed thermal energy storage (TES) systems using alumina, steel, and hybrid particles as sensible heat storage media. The study employed the Taguchi method and composite desirability function to optimize the design and operation of a CSP–CO_2 Rankine plant, with a focus on capacity factor and thermal output. Abdulla and Reddy [15], developed a dynamic 2D, two-phase model to simulate heat transfer in a molten salt-packed-bed thermocline thermal energy storage (TES) system for concentrating solar power (CSP) applications. They examined how factors like filler diameter, inlet salt velocity, and operating temperature range affect discharge efficiency and thermocline thickness. Kocak and Paksoy [16], explored a low-cost, eco-friendly material for thermal energy storage in a small-scale system operating below 200 °C for industrial solar applications. Through experimental and numerical analysis, they evaluated performance under varying charging temperatures and fluid velocities.

This study presents and assesses a TCC power plant using solar energy as its primary source. The proposed power station incorporates rock bed energy storage to maintain steady power generation, especially during periods of minimal sunshine. The study assesses the exergy efficiency, exergy destruction, initial investment costs, and expenses for all components in a TCC. Parametric analyses evaluate the impact of altering state characteristics and operational variables on the net overall efficiency and particular costs of the TCC. This research is unique in that it performs a performance and exergoeconomic analysis of a solar-based TCC with a rock-bed thermal storage unit. It also examines how changing parameters affect the system's effectiveness and expenses.

2. System description

The TCC integrates a primary Brayton cycle with two secondary cycles: the Rankine cycle (RC) and the organic Rankine cycle (ORC). This study focuses on the Salahaddin region in Iraq, utilizing site-specific data for system analysis. A schematic representation of the proposed system is illustrated in Figure 1. The power plant operates using both solar energy and fuel, optimizing energy utilization through heliostats, solar receivers, a gas turbine cycle (GTC), rock bed thermal energy storage (RBTES), and the secondary Rankine and Organic Rankine Cycle (ORC) cycles. Using a compressor, the system pressurizes ambient air to 1.62 MPa, then heats it in a solar central receiver. A combustion chamber stabilizes the gas turbine inlet temperature during charging to compensate for variations in solar energy. The rock bed thermal storage system accumulates excess heat, enabling electricity generation at night when solar input is unavailable. Achieving gas turbine inlet temperatures of up to 1000°C would significantly enhance efficiency. The Rankine cycle utilizes the hot exhaust gases from the gas turbine, storing residual heat in the rock bed storage system. In contrast, the organic Rankine cycle recovers additional heat from the stored air. The Brayton cycle operates for 10 hours daily, maximizing the utilization of direct solar radiation. In contrast, the Rankine cycle sustains electricity production for the remaining 14 hours, ensuring a continuous power supply throughout the day.

Thermodynamic and thermoeconomic analyses were conducted under defined assumptions to ensure accuracy and consistency. Reference conditions were set at 1 bar and 25 °C, with kinetic and potential energy effects considered negligible. The system was modeled under steady-state conditions, assuming stable solar input. Each cycle utilized a specific working fluid (air for the Brayton cycle, water for the Rankine cycle, and R600a for the organic Rankine cycle) to optimize thermodynamic performance. The compressor, pump, and turbines are assumed to operate adiabatically, meaning heat losses to the surroundings are negligible. Additionally, the sun's temperature is estimated at 6,000 K, which is the thermal energy source for the solar receivers and heliostat field, driving the system's power generation processes. These assumptions provide a controlled framework for evaluating the energy, exergy, and economic performance of the integrated system. All thermodynamic modeling, performance simulations, and parametric analyses were conducted using Engineering Equation Solver (EES) software. This study is based entirely on numerical simulation and does not include practical experimentation. Monthly and seasonal variations in solar radiation and ambient temperature were obtained from the NASA Surface Meteorology and Solar Energy database for the Salahaddin region in Iraq. These values were used as inputs in the EES software to assess system performance across different months of the year. Although this study uses weather and solar radiation data from Salahaddin, Iraq, the system is designed to be scalable and adaptable to other regions with similar solar potential. The simulation is based on monthly average daily solar radiation values, which implicitly account for day length and solar intensity.

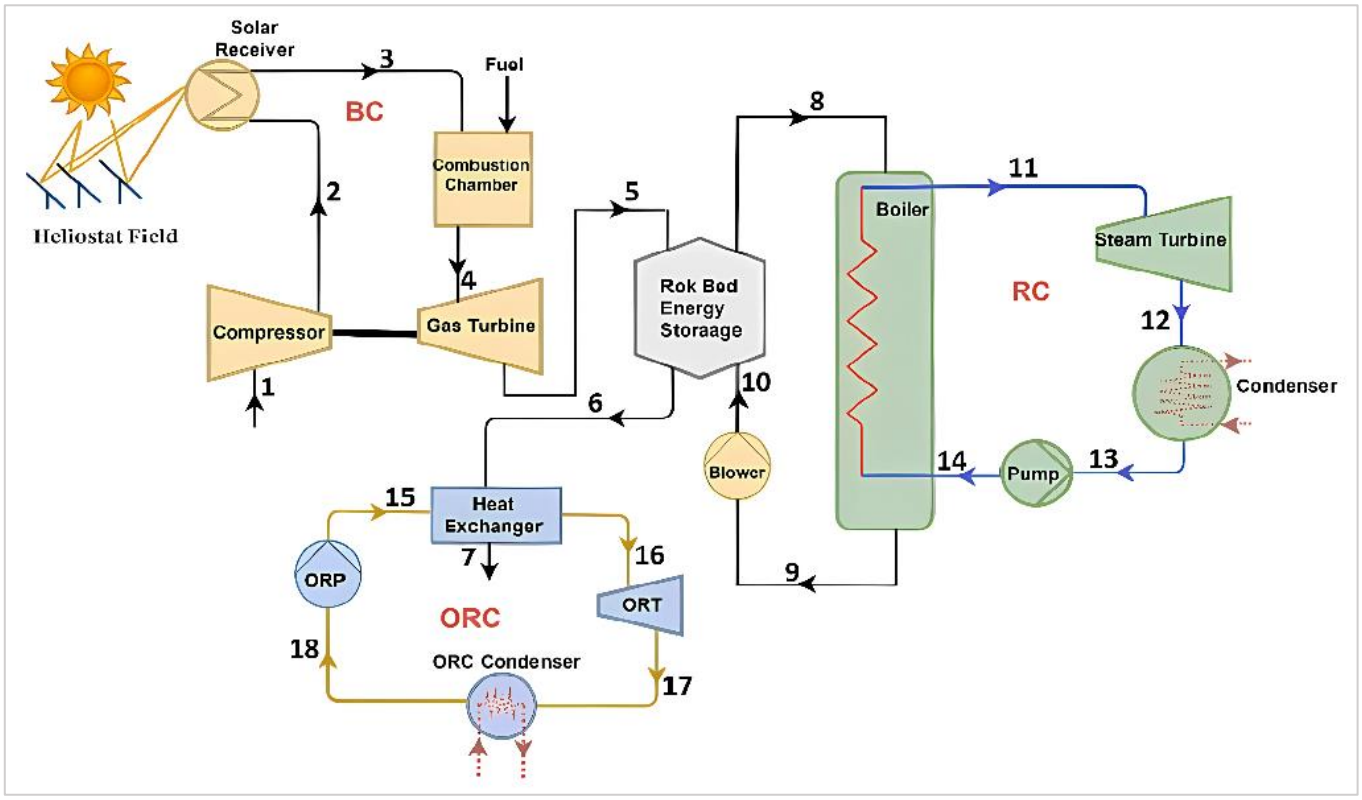

Figure 1: Schematic diagram of the triple cycle power plant

The TCC is analyzed through individual thermodynamic modeling of each component, ensuring a comprehensive evaluation of system performance. The analysis incorporates mass, energy, and exergy balance equations, as well as thermo-economic assessments, to determine efficiency and cost-effectiveness. These equations are applied to quantify energy flows, exergy destruction, and economic feasibility across the Brayton, Rankine, and organic Rankine cycles. The study also considers key operational and technical parameters detailed in Table 1, providing essential reference values for system optimization. This modeling approach enables an in-depth understanding of how components interact and contribute to overall system efficiency, facilitating performance improvements and sustainable energy utilization.

Table 1: Operation conditions used for the TCC

Component	Parameter	Value
AC	Compression ratio	14.5
	Inlet temperature	33.65 ℃
	Inlet pressure	101.3 kPa
	Isentropic efficiency	84%
	Air flow rate	52 m^3
Heliostats field	Area	53935 m^2
GT	Inlet temperature	1000 ℃
	Isentropic efficiency	85%
ST	Inlet pressure	5000 kPa
	Isentropic efficiency	80%
Condenser	Condenser temperature	60 ℃
Pump	Isentropic efficiency	90%
ORC	Inlet pressure	1700 kPa
	Isentropic efficiency	85
ORC-Cond	Condenser pressure	635.7 kPa
ORP	Isentropic efficiency	90%

In this study, a parametric optimization strategy was employed. The objective functions include maximizing energy and exergy efficiency, as well as minimizing both exergy destruction and levelized electricity cost. Key design and operational parameters, such as pressure ratio, ambient temperature, and gas turbine inlet temperature, were varied within practical limits. Simulations were performed for each combination of parameters, and results were evaluated to determine optimal operating conditions. Figure 2 presents the flowchart of the optimization framework.

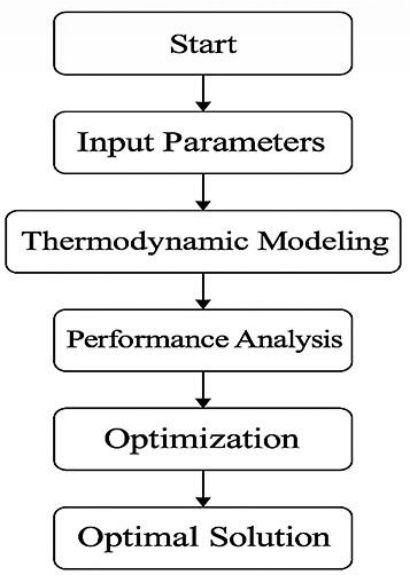

Figure 2: Flowchart of the optimization framework

3. Thermodynamic analysis

The system's mass balance equation is expressed by Equation1:

$$\sum \dot{m}_{in} = \sum \dot{m}_{out} \tag{1}$$

Equation 2 represents the system's overall energy balance [17, 18]:

$$\dot{Q}_{in} + \dot{W}_{in} + \sum \dot{m}_{in} h_{\text{in}} = \dot{Q}_{out} + \dot{W}_{out} + \sum \dot{m}_{out} h_{out} \tag{2}$$

The overall exergy balance equation for the system can be expressed as shown in Equations 3-5 [19, 20]:

$$\sum (\dot{m}ex)_{in} + \dot{E}x_{in,W} + \dot{E}x_{in,Q} = \sum (\dot{m}ex)_{out} + \dot{E}x_{\text{out},W} + \dot{E}x_{\text{out},Q} \tag{3}$$

$$\dot{E}^{Q} = \dot{Q}\left(1 - \frac{T_0}{T}\right) \tag{4}$$

$$\dot{m}_{in} S_{in} + \left(\frac{\dot{Q}}{T}\right) + \dot{S}_{gen} = \dot{m}_{out} S_{out} \tag{5}$$

The heat transfer rate between the solar receiver and the air can be calculated using the Equations 6 and 7 [19, 21]:

$$\dot{Q}_{\text{Solar}} = \dot{Q}_h - \dot{Q}_{\text{rec,loss}} \tag{6}$$

$$\dot{Q}_{Solar} = \dot{m}_3 h_3 - \dot{m}_2 h_2 = \dot{m}_3 c_{p,3} T_3 - \dot{m}_2 c_{p,2} T_2 \tag{7}$$

The Equations 8 and 9 can calculate the heat transfer rate in the heliostat field and the receiver heat loss rate [22]:

$$\dot{Q}_h = A_h \times N \times I \times \eta_h \tag{8}$$

$$\dot{Q}_{rec,loss} = \dot{Q}_{conv} + \dot{Q}_{rad} = A_r \times [h_c \times (T_r - T_0) + \sigma \times \varepsilon \times (T_r^4 - T_0^4)] \tag{9}$$

The convective heat transfer coefficient of air (h_c) in W/m^{2}K units can be determined using Equation10 [23]:

$$h_c = 10.45 - V + 10\sqrt{V} \tag{10}$$

The gas turbine cycle's outlet temperature and power consumption of the compressor are determined using the Equations 11 and 12 [24]:

$$T_{\text{out}} = T_{\text{in}} \left(1 + \frac{1}{\eta_{AC}} \left(P_{r,AC}^{\frac{k_{air}-1}{k_{air}}} - 1\right)\right) \tag{11}$$

$$\dot{W}_{AC} = \dot{m}_{air} * (h_{\text{out}} - h_{in}) \quad (12)$$

$P_{r,AC}$ and η_{AC} are the pressure ratio of the compressor and the isentropic efficiency of the compressor, respectively, and k_{air} and $\dot{m}_{air}$ are the specific heat rate of the air and the mass flow rate of the air (in kg/s), respectively. The gas turbine output temperature and the power generated in the turbine are determined using Equations 13-15 [25, 26]:

$$T_{GT,\text{ out}} = T_{GT,\text{ in}} \left(1 - \eta_{GT}\left(1 - P_{r,GT}^{\frac{1-k_{air}}{k_{air}}}\right)\right) \quad (13)$$

$$\dot{W}_{GT} = \dot{m}_{GT,in} * \left(h_{GT,\,in} - h_{GT,\,out}\right) \quad (14)$$

$$\dot{W}_{GT,net} = \eta_{GEN} * \left(\dot{W}_{GT} - \dot{W}_{AC}\right) \quad (15)$$

$P_{r,AC}$, η_{AC} , η_{GEN}, k_{air} and $\dot{m}_{GT,in}$ used in the equation respectively denote the turbine pressure ratio, isentropic efficiency of the turbine, generator efficiency, specific heat ratio for air, and flow rate of the combustion gases (in kg/s).

The thermodynamic model for calculating the thermal energy storage tank involves determining the heat loss from the tank to the environment. The total heat loss coefficient (U) from the store to the ambient air is computed first, followed by the calculation of the total heat loss using the provided Equation 16 [12, 27]:

$$\dot{Q}_{\text{loss}} = U \times A \times (T_m - T_0) \quad (16)$$

where A is the total surface area of the rock bed storage tank (in m^2), T_m the mean temperature (in °C), and T_0 the ambient temperature (in °C). The thermal energy storage tank operates in three distinct modes: charging, discharging, and storage. The following formulae determine the total energy stored during charging (Equations 17 and 18) [12]:

$$Q_{\text{charging}} = (m_5 h_5 - m_6 h_6) \times 3600 \times t_{charging} \quad (17)$$

$$Q_{\text{charging}} = m_{rock}\, c_{rock} (T_5 - T_0) \quad (18)$$

where $t_{charging}$ is the charging time, c_{rock} the specific heat of the rock (c_{rock} =0.840 kJ/kg K), and m_{rock} the mass of the rock. Equation 19 is utilized to calculate the total heat loss throughout the storage time.

$$Q_{\text{charging}} = Q_{\text{discharging}} + Q_{\text{loss}} \quad (19)$$

The heat transported to the multi-generation system during the discharge time is determined using the following calculation (Equations 20 and 21) [12]:

$$Q_{\text{discharging}} = (m_8 h_8 - m_{10} h_{10}) \times 3600 \times t_{\text{discharging}} \quad (20)$$

$$Q_{\text{discharging}} = m_{\text{rock}}\, c_{\text{rock}}\, (T_5 - T_0) \quad (21)$$

where $t_{\text{discharging}}$ is the discharging time. Table 2 displays the energy and exergy formulae for the components utilized in the system. Table 3 displays the exergy of fuel and product for each component.

The efficiency of the TCC can be calculated by analyzing the first and second laws as shown in Equations 22 and 23 [28, 29]:

$$\eta_{\text{I}} = \frac{\dot{W}_{\text{net}}}{\dot{Q}_{\text{in}}} \quad (22)$$

$$\eta_{II} = \frac{\dot{W}_{net}}{\dot{E}x_{in}} \quad (23)$$

The power output of the TCC can be determined as follows in Equation 24:

$$\dot{W}_{\text{net}} = \dot{W}_{\text{GT}} - \dot{W}_{\text{Comp}} + \dot{W}_{ST} - \dot{W}_{\text{Pump}} - \dot{W}_{\text{Blower}} + \dot{W}_{ORT} - \dot{W}_{\text{ORP}} \quad (24)$$

The system's heat and exergy input can be calculated as follows in Equation 25 and 26:

$$\dot{Q}_{in} = \dot{Q}_{Fuel} + \dot{Q}_{\text{Solar}} \quad (25)$$

$$\dot{E}x_{in} = \dot{E}x_{Q,Fuel} + \dot{E}x_{Solar} \quad (26)$$

Table 2: Equations for energy and exergy balancing in the TCC power plant

Component	Energy Balance Equation	Exergy Balance Equation
AC	$\dot{m}_1 h_1 + \dot{W}_{AC} = \dot{m}_2 h_2$	$\dot{E}_{D,AC} = (\dot{E}_1 - \dot{E}_2) + \dot{W}_{AC}$
Blower	$\dot{m}_9 h_9 + \dot{W}_{blower} = \dot{m}_{10} h_{10}$	$\dot{E}_{D,blower} = (\dot{E}_9 - \dot{E}_{10}) + \dot{W}_{blower}$
Boiler	$\dot{m}_8(h_8 - h_9) = \dot{m}_{11}(h_{11} - h_{14})$	$\dot{E}_{\mathrm{D,Boiler}} = \dot{E}_8 - \dot{E}_9 + \dot{E}_{14} - \dot{E}_{11}$
CC	$\dot{m}_3 h_3 + \eta_{CC}\dot{m}_{\mathrm{f}}\mathrm{LHV}_f = \dot{m}_4 h_4$	$\dot{E}_{\mathrm{D,CC}} = \dot{E}_3 + \dot{E}_{Q,Fuel} - \dot{E}_4$
Condenser	$\dot{m}_{12}(h_{12} - h_{13}) = \dot{m}_{19}(h_{20} - h_{19})$	$\dot{E}_{\mathrm{D,cond}} = \dot{E}_{12} - \dot{E}_{13} + \dot{E}_{19} - \dot{E}_{20}$
GT	$\dot{m}_4 h_4 = \dot{m}_5 h_5 + \dot{W}_{GT}$	$\dot{E}_{D,GT} = (\dot{E}_4 - \dot{E}_5) - \dot{W}_{GT}$
HE	$\dot{m}_6(h_6 - h_7) = \dot{m}_{15}(h_{16} - h_{15})$	$\dot{E}_{\mathrm{D,HE}} = \dot{E}_6 - \dot{E}_7 + \dot{E}_{15} - \dot{E}_{16}$
ORC-Cond	$\dot{m}_{17}(h_{17} - h_{18}) = \dot{m}_{21}(h_{21} - h_{22})$	$\dot{E}_{\mathrm{D,ORC-Cond}} = \dot{E}_{17} - \dot{E}_{18} + \dot{E}_{21} - \dot{E}_{22}$
ORP	$\dot{m}_{18} h_{18} + \dot{W}_{ORP} = \dot{m}_{15} h_{15}$	$\dot{E}_{D,ORP} = (\dot{E}_{18} - \dot{E}_{15}) + \dot{W}_{ORP}$
ORT	$\dot{m}_{16} h_{16} = \dot{m}_{17} h_{17} + \dot{W}_{ORT}$	$\dot{E}_{D,ORT} = (\dot{E}_{16} - \dot{E}_{17}) - \dot{W}_{ORT}$
Pump	$\dot{m}_{13} h_{13} + \dot{W}_{pump} = \dot{m}_{14} h_{14}$	$\dot{E}_{D,pump} = (\dot{E}_{13} - \dot{E}_{14}) + \dot{W}_{pump}$
RBES Charging	$(m_5 h_5 - m_6 h_6) \times 3600 \times t_{charging} = m_{rock}\, c_{rock}(T_5 - T_0)$	$(\dot{E}_5 - \dot{E}_6) \times 3600 \times t_{\mathrm{charging}} = m_{\mathrm{rock}}\, c_{\mathrm{rock}} \left((T_5 - T_0) - T_0 \times \ln\left(\frac{T_5}{T_0}\right)\right) + \dot{E}_{D,\mathrm{charging}} \times 3600 \times t_{\mathrm{charging}}$
RBES Discharging	$(m_8 h_8 - m_{10} h_{10}) \times 3600 \times t_{\mathrm{discharging}} = m_{rock}\, c_{rock}(T_5 - T_0)$	$(\dot{E}_8 - \dot{E}_{10}) \times 3600 \times t_{\mathrm{discharging}} + \dot{E}_{D,\mathrm{discharging}} \times 3600 \times t_{\mathrm{discharging}} = m_{\mathrm{rock}}\, c_{\mathrm{rock}} \left((T_5 - T_0) - T_0 \times \ln(T_5/T_0)\right)$
SR	$\dot{m}_2 h_2 + \dot{Q}_{SR} = \dot{m}_3 h_3$	$\dot{E}_{D,SR} = (\dot{E}_2 - \dot{E}_3) + \dot{E}_{Q,Solar}$
ST	$\dot{m}_{11} h_{11} = \dot{m}_{12} h_{12} + \dot{W}_{ST}$	$\dot{E}_{D,ST} = (\dot{E}_{11} - \dot{E}_{12}) - \dot{W}_{ST}$

Table 3: Product and fuel exergy equations

Component	Fuel Exergy Equation	Product Exergy Equation
AC	$\dot{W}_{AC}$	$\dot{E}_2 - \dot{E}_1$
Blower	$\dot{W}_{blower}$	$\dot{E}_{10} - \dot{E}_9$
Boiler	$\dot{E}_8 - \dot{E}_9$	$\dot{E}_{11} - \dot{E}_{14}$
CC	$\dot{E}_{Q,Fuel}$	$\dot{E}_4 - \dot{E}_3$
Condenser	$\dot{E}_{12} - \dot{E}_{13}$	$\dot{E}_{20} - \dot{E}_{19}$
GT	$\dot{E}_4 - \dot{E}_5$	$\dot{W}_{GT}$
HE	$\dot{E}_6 - \dot{E}_7$	$\dot{E}_{16} - \dot{E}_{15}$
ORC-Cond	$\dot{E}_{17} - \dot{E}_{18}$	$\dot{E}_{22} - \dot{E}_{21}$
ORP	$\dot{W}_{ORP}$	$\dot{E}_{15} - \dot{E}_{18}$
ORT	$\dot{E}_{16} - \dot{E}_{17}$	$\dot{W}_{ORT}$
Pump	$\dot{W}_{pump}$	$\dot{E}_{14} - \dot{E}_{13}$
RBES Charging	$\dot{E}_5 - \dot{E}_6$	$m_{\mathrm{rock}}\, c_{\mathrm{rock}} \left((T_5 - T_0) - T_0 \times \ln\left(\frac{T_5}{T_0}\right)\right) / (3600 \times t_{\mathrm{charging}})$
RBES Discharging	$m_{\mathrm{rock}}\, c_{\mathrm{rock}} \left((T_5 - T_0) - T_0 \times \ln\left(\frac{T_5}{T_0}\right)\right) / (3600 \times t_{\mathrm{discharging}})$	$\dot{E}_8 - \dot{E}_{10}$
SR	$\dot{E}_{Q,Solar}$	$\dot{E}_3 - \dot{E}_2$
ST	$\dot{E}_{11} - \dot{E}_{12}$	$\dot{W}_{ST}$

4. Exergy economic analysis

The general equation for the exergy-cost balance of each component in the system can be expressed as follows (Equation 27) [30]:

$$\sum \dot{C}_{in,k} + \dot{C}_{Qk} + \dot{Z}_k = \sum \dot{C}_{out,k} + \dot{C}_{w,k} \quad (27)$$

The heat and power exergy cost flows are denoted as $\dot{C}_{Qk}$, and $\dot{C}_{w,k}$ correspondingly, whereas $\dot{Z}_k$ represents the capital cost, operation, and maintenance cost flow. The calculation of $\dot{Z}_k$ is based on the formula shown in Equation 28 [31]:

$$\dot{Z}_k = Z_k^{CI} * CRF * \frac{\phi}{t} \quad (28)$$

The variables Z_k^{CI}, CRF, ϕ and t in the equation represent the investment cost of the components, the return on capital factor, and the maintenance factor, respectively, as well as the annual operating time of the system. In this study, the total annual working time is assumed to be 8,640 hours. The CRF value is calculated by Equation 29 [32]:

$$CRF = \frac{i(1+i)^N}{(1-i)^N - 1} \quad (29)$$

The interest rate i is accepted as 12%, and N is the total system life of 20 years [33]. The exergy cost flow for each location in the system is determined using the Equation 30:

$$\dot{C} = c\dot{E}x \quad (30)$$

$\dot{E}x$ denotes exergy current and c denotes the specific exergy cost. The system's performance is evaluated using the exergy-economic factor, designated as f_k, determined by the Equation 31 [34, 35]:

$$f_k = \frac{\dot{Z}_k}{\dot{Z}_k + \dot{C}_{D,k}} \quad (31)$$

The exergy destruction costs, denoted as $\dot{C}_{D,k}$ is determined using the Equation 32 [36]:

$$\dot{C}_{D,k} = c_f \dot{E}x_{D,k} \quad (32)$$

$\dot{E}x_{D,k}$ is the exergy destruction. All the supplementary equations identified with the cost equilibrium equations are listed in Table 4. The total cost of the system ($\dot{C}_{system}$) can be calculated using the Equation 33 [37]:

$$\dot{C}_{system} = \sum \dot{z}_k + \sum \dot{C}_{D,k} \quad (33)$$

The system's unit cost of electricity produced ($\dot{C}_{electricity}$) is another important aspect in the cost analysis. Equation 34 provided calculates the overall cost of the power generated [37]:

$$\dot{C}_{electricity} = \frac{\dot{C}_{system}}{\dot{W}_{NET}} \quad (34)$$

Table 4: Cost balance equations for the system elements

Component	Cost Flow Equations	Auxiliary Equations
AC	$\dot{C}_1 + \dot{C}_{AC} + \dot{Z}_{AC} = \dot{C}_2$	$c_1 = 0$
SR	$\dot{C}_2 + \dot{Z}_{hel} = \dot{C}_3$	$c_2 = c_3$
CC	$\dot{C}_3 + \dot{C}_{fuel} + \dot{Z}_{CC} = \dot{C}_4$	$c_3 = c_4$ $c_f = 12$
GT	$\dot{C}_4 + \dot{Z}_{GT} = \dot{C}_5 + \dot{C}_{GT}$	$c_4 = c_5$ $c_{AC} = c_{GT}$
RBES	$\dot{C}_5 + \dot{C}_{10} + \dot{Z}_{RBES} = \dot{C}_6 + \dot{C}_8$	$c_5 = c_6$
Blower	$\dot{C}_9 + \dot{C}_{Blower} + \dot{Z}_{Blower} = \dot{C}_{10}$	$c_{blower} = c_{GT}$
Boiler	$\dot{C}_8 + \dot{C}_{14} + \dot{Z}_{Boiler} = \dot{C}_9 + \dot{C}_{11}$	$c_8 = c_9$
ST	$\dot{C}_{11} + \dot{Z}_{ST} = \dot{C}_{12} + \dot{C}_{ST}$	$c_{12} = c_{11}$
Condenser	$\dot{C}_{12} + \dot{C}_{19} + \dot{Z}_{Condenser} = \dot{C}_{13} + \dot{C}_{20}$	$c_{12} = c_{13}$ $c_{10} = 0$
Pump	$\dot{C}_{13} + \dot{C}_{Pump} + \dot{Z}_{pump} = \dot{C}_{14}$	$c_{Pump} = c_{ST}$
HE	$\dot{C}_6 + \dot{C}_{15} + \dot{Z}_{HE} = \dot{C}_7 + \dot{C}_{16}$	$c_7 = 0$
ORT	$\dot{C}_{16} + \dot{Z}_{ORT} = \dot{C}_{17} + \dot{C}_{ORT}$	$c_{16} = c_{17}$
ORC-Cond	$\dot{C}_{17} + \dot{C}_{21} + \dot{Z}_{ORC-Cond} = \dot{C}_{18} + \dot{C}_{22}$	$c_{17} = c_{18}$ $c_{21} = 0$
ORP	$\dot{C}_{18} + \dot{C}_{ORP} + \dot{Z}_{ORP} = \dot{C}_{14}$	$c_{ORP} = c_{ORT}$

5. Results and discussion

The bar chart in Figure 3 validates the present thermodynamic model by comparing its results with those from the published work of Öztürk et al., [12]. The comparison focuses on the net power output (MW) of two main cycle components: the Gas Turbine (GT) power and the Rankine Cycle (RC) power. The results demonstrate a high level of agreement between the two models, with only minor deviations. The present model predicts a GT power of 3.865 MW, while the Öztürk et al. [12], model

reports 3.87 MW, showing a negligible difference of 0.005 MW (0.13%). Similarly, for the RC power, the present model calculates 1.757 MW, compared to 1.76 MW in the reference model, with a minimal discrepancy of 0.003 MW (0.17%). The minor differences confirm that the current model accurately replicates published results, demonstrating its reliability and suitability for further thermodynamic analysis.

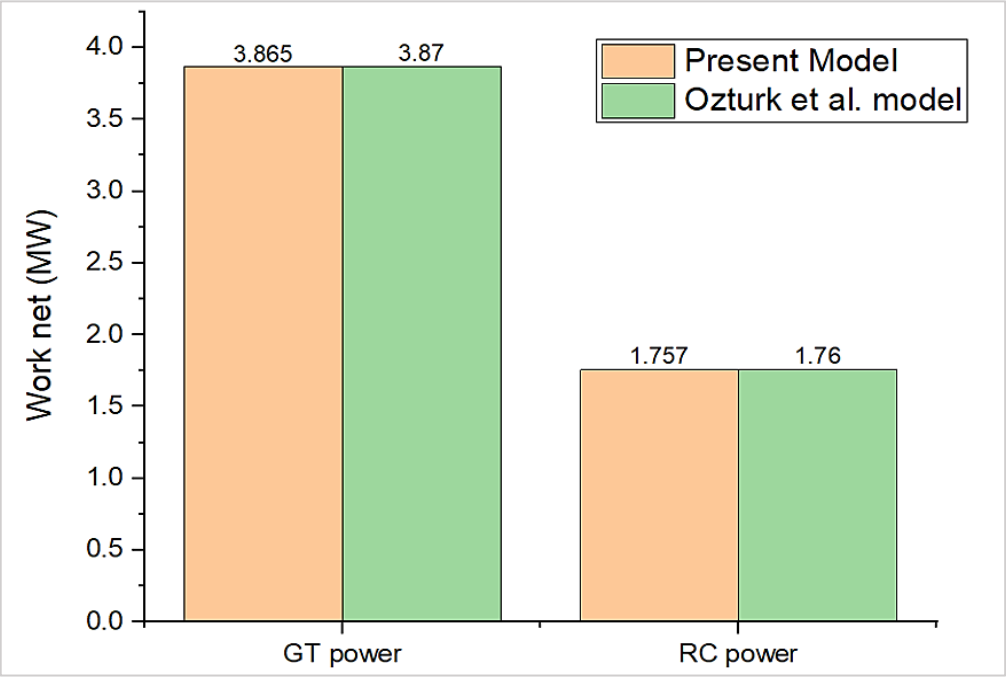

Figure 3: Validation of the present thermodynamic model with published work by Öztürk et al. [12]

Table 5 outlines the thermodynamic properties of the solar-based triple combined cycle under optimal conditions, detailing temperature, pressure, enthalpy, entropy, exergy, and cost across various states.

Table 5: Thermodynamic properties for each state of the solar-based TCC under optimal conditions

State	$\dot{m}$ (kg/s)	P (kPa)	T (°C)	S (KJ/kg. K)	h (kJ/kg)	$\dot{E}$ (MW)	$\dot{C}$ ($/h)	c ($/GJ)
1	52	101.3	306.7	5.724	307.1	0.0633	0	0
2	52	1469	711.7	5.823	726.2	20.33	117.4	1.604
3	52	1469	1172	6.383	1245	38.64	223.1	1.604
4	52	1469	1273	6.48	1364	43.31	427.5	2.742
5	52	108.8	752.1	6.63	770	10.1	99.68	2.742
6	52	101.3	382.3	5.946	383.4	0.5848	5.773	2.742
7	52	101.3	330.9	5.801	331.5	0.1439	0	0
8	37.51	107	742.1	6.62	759.1	6.986	113.2	4.503
9	37.51	107	343.2	5.822	343.9	0.3334	5.404	4.503
10	37.51	140	375.3	5.835	376.3	1.403	19.04	3.769
11	5.092	5000	722.1	6.818	3315	6.557	155.6	6.592
12	5.092	19.81	333	7.46	2459	1.222	29.01	6.592
13	5.092	19.81	333	0.8294	250.6	0.0407	0.966	6.592
14	5.092	5000	333.2	0.8311	256.2	0.0668	2.61	10.86
15	44.91	1700	315.9	1.15	245.2	0.0761	10.71	39.1
16	44.91	1700	370.3	1.324	305.3	0.4398	40.58	25.63
17	44.91	164.3	315	1.327	300	0.1629	15.03	25.63
18	44.91	164.3	315	1.149	243.9	0.0268	2.47	25.63
19	269	101.3	306.7	0.4847	140.4	0.139	0	0
20	269	101.3	316.7	0.6189	182.2	0.6315	28.19	12.4
21	60.36	101.3	306.7	0.4847	140.4	0.0312	0	0
22	60.36	101.3	316.7	0.6189	182.2	0.1417	13.8	27.05

Table 6 and Figure 4 illustrate the distribution of exergy destruction across the components of the solar-based TCC system under optimal conditions. The highest exergy destruction (7.346 MW) occurs in the solar receivers due to the large temperature differentials. Significant contributions also come from the gas turbines (13.84%) and combustion chambers (10.31%). Figure 3 highlights substantial losses in the GT, which are caused by high-temperature air and associated irreversibilities. The rock bed energy storage system accounts for 10.03% of exergy destruction due to thermal losses during charge/discharge cycles.

Components such as air compressors, condensers, and steam turbines show moderate losses, while pumps and heat exchangers contribute minimally, indicating good thermal performance. Notably, the boiler achieves a high exergy efficiency of 97.6%.

Table 6: The exergy analysis of the solar-based TCC components

Component	$\dot{E}_{input}$ (MW)	$\dot{E}_{output}$ (MW)	$\dot{E}_{destruction}$ (MW)	$\dot{E}_{destruction}$ (%)	Exergy efficiency (%)
AC	21.97	20.3	1.53	9.1	93
SR	25.7	18.3	7.35	43.9	100
CC	6.39	4.67	1.72	10.3	73.1
GT	33.21	30.9	2.31	13.84	93.03
RBES	15.15	13.47	1.677	10.03	88.9
RBES Charging	9.51	7.89	1.624	9.714	82.9
RBES Discharging	5.64	5.58	0.053	0.32	99.1
Boiler	6.65	6.5	0.162	0.97	97.6
ST	5.34	4.36	0.957	5.84	81.72
Condenser	1.18	0.492	0.69	4.12	41.7
Pump	0.029	0.026	0.0026	0.015	91.1
Blower	1.22	1.1	0.146	0.87	88.03
ORT	0.277	0.237	0.0396	0.237	85.7
ORC-Cond	0.136	0.111	0.026	0.153	81.2
Heat exchanger	0.441	0.364	0.077	0.462	82.5
ORP	0.061	0.049	0.0114	0.0684	81.2
Total			16.7		

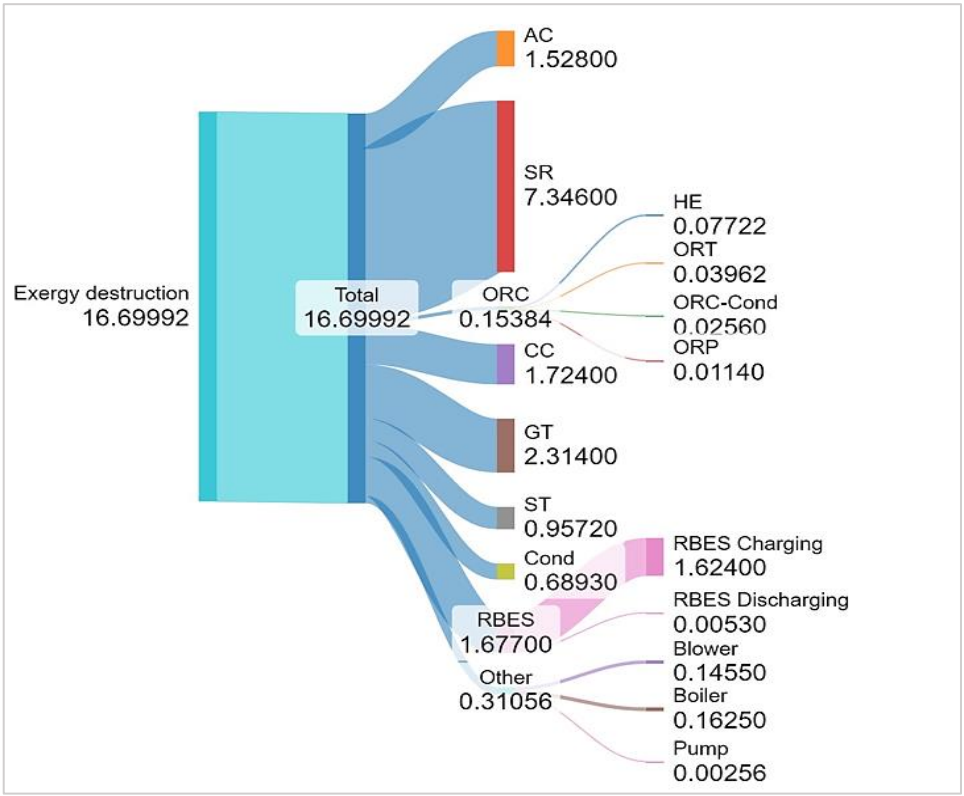

Figure 4: Exergy degradation rates of system components

Table 7 presents the exergoeconomic analysis of the solar-based triple combined cycle, detailing the cost distribution across system components. The solar receiver exhibits the highest capital cost rate of $105.8/hr, primarily due to its vital role and high material and installation costs. The steam turbine ($56.09/h) and combustion chamber ($55.23/h) follow. The boiler, air compressor, and gas turbine also incur notable costs. Moderate capital costs are observed for components such as the rock bed energy storage (RBES), heat exchanger (HE), and organic Rankine turbine (ORT), ranging from $10.69 to $ 24.10/h, which indicates their secondary cost impact. In addition to capital costs, the exergy destruction cost rate is a critical element in exergoeconomic analysis. The combustion chamber incurs the highest exergy destruction cost at $55.07 per hour, followed by the gas turbine, which indicates major irreversibilities and thermal losses. Overall, capital costs exceed the total exergy destruction costs, highlighting the dominance of investment expenses. The solar receiver has the highest combined cost of capital and exergy destruction (Ż_k + Ċ_D), followed by the steam turbine, which highlights their economic importance. The system achieves a notable exergoeconomic factor of 64.58%, which reflects a strong balance between efficiency and cost.

Table 7: Exergo-economic outcomes of components of solar-based TCC

Component	c_f ($/GJ)	c_p ($/GJ)	$\dot{C}_D$ ($/h)	$\dot{Z}_K$ ($/h)	$\dot{Z}_K + \dot{C}_D$ ($/h)	f (%)
AC	1.02	1.61	5.625	37.19	42.82	86.86
SR	-	1.604	-	105.8	105.8	100
CC	8.88	12.16	55.07	0.16	55.23	0.302
GT	2.724	3.061	22.84	12.62	35.46	35.59
RBES	1.722	1.942	10.39	0.3	10.69	2.816
Boiler	4.503	6.549	2.634	45.336	47.97	94.94
ST	6.592	10.17	23.15	32.94	56.09	58.74
Condenser	6.592	15.9	16.36	0.14	16.5	0.8516
Pump	10.17	17.52	0.0937	0.5962	0.6899	86.42
Blower	3.061	3.54	1.603	0.244	1.847	13.18
ORT	25.63	36.96	3.656	6.021	9.677	62.22
ORC-Cond	25.63	34.68	2.362	1.239	3.601	34.41
HE	3.637	22.81	1.011	24.089	25.1	95.97
ORP	36.96	46.4	1.521	0.157	1.678	9.381
Total System			140.7	266.83	412.9	64.58

Figures 5a and 5b illustrate the impact of ambient temperature (T_1) on key performance metrics of the solar-based TCC. As T_1 increases, a decline is observed in net power output ($\dot{W}_{net}$), system power cost rate ($\dot{C}_{electricity}$), first-law efficiency (η_I), and second-law efficiency (η_{II}). This trend is primarily attributed to the increase in enthalpy (h_2) and higher power consumption of the air compressor, which reduces the net work available for electricity generation. Since the compressor consumes a portion of $\dot{W}_{net}$, the increase in air compressor work ($\dot{W}AC$) negatively affects both the net power output and overall efficiency. As shown in Figure 5a, $\dot{W}_{net}$ decreases from 14,285 kW to 12,026 kW when T_1 rises from 280 K to 312 K, demonstrating a clear reduction in system performance under higher ambient temperatures.

Interestingly, despite the decline in power output, the total system cost rate and electricity generation cost experience a slight reduction. This is due to lower capital, maintenance, and operational costs, which decrease the specific cost per unit of electricity produced. Figure 5a highlights this effect, showing a reduction in $\dot{C}_{electricity}$ from 35.73 $/MWh to 32.91 $/MWh as T_1 increases within the given range. Furthermore, Figure 5b illustrates the corresponding decline in system efficiencies. The first-law efficiency (η_I), which represents the overall thermal efficiency, decreases from 39.14% to 36.98%. In contrast, the second-law efficiency (ηII), which measures the system's ability to utilize available energy effectively, drops from 43.37% to 40.23%.

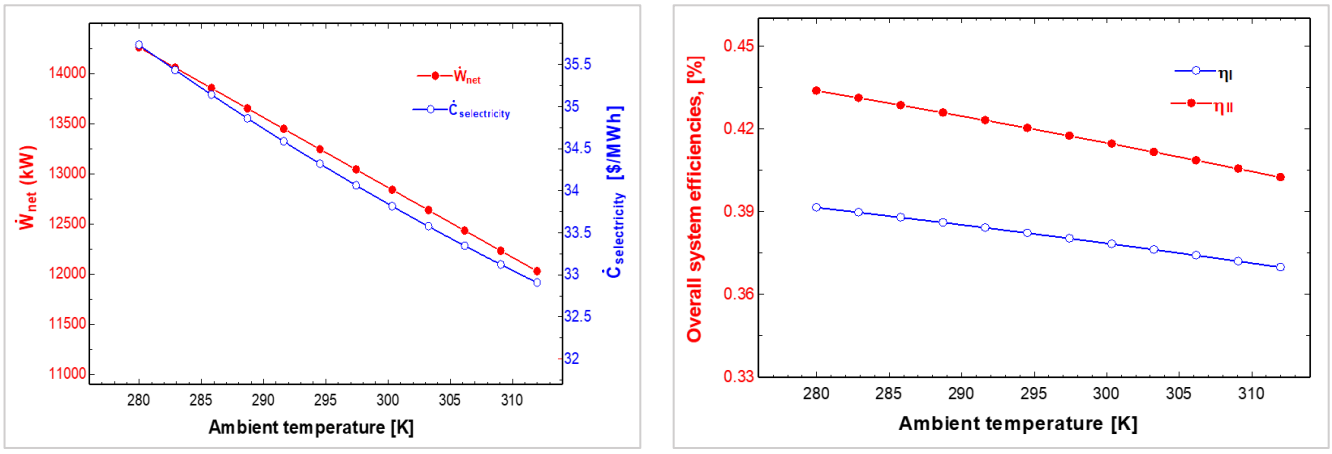

(a) **(b)**

Figure 5: The system's work output, a) power cost rate, and b) overall system efficiencies as a function of ambient temperature change

Figures 6a and 6b analyze the effect of the pressure ratio (PR) on the performance, cost, and efficiency of the solar-based triple combined cycle system. The results show that the system's net power output ($\dot{W}_{net}$) decreases as PR increases. Specifically, when PR increases from 8 to 20, $\dot{W}$net decreases from 14,215 kW to 10,026 kW, reflecting a significant reduction of approximately 4,189 kW. This decline is primarily attributed to the higher work requirement of the air compressor, which offsets the available power output. A notable trend emerges when PR reaches 16.4, where the system's electricity cost rate decreases, dropping from 34.57 $/hr. This cost reduction is due to the simultaneous decrease in $\dot{W}_{net}$ and the fuel input rate, which helps balance the system's economic performance. However, beyond PR = 16.4, the electricity cost rate begins to increase, driven by the substantial decline in $\dot{W}_{net}$, which reduces power generation efficiency and raises the cost per unit of electricity.

Figure 6b illustrates that efficiency trends follow a peak behavior. Initially, as pressure ratio (PR) increases, both first-law efficiency (η_I) and second-law efficiency (η_{II}) improve, reaching their maximum values at 14.5 bar, where η_I and η_{II} peak at 37.37% and 40.8%, respectively. Beyond this optimal PR value, system efficiency declines due to excessive compressor work and reduced net power output, which outweighs any efficiency gains. These findings suggest that optimizing the pressure ratio

is crucial for maintaining high efficiency and economic viability. Operating at an optimal power ratio (PR) of 14.5–16.4 ensures maximum efficiency while keeping electricity costs low.

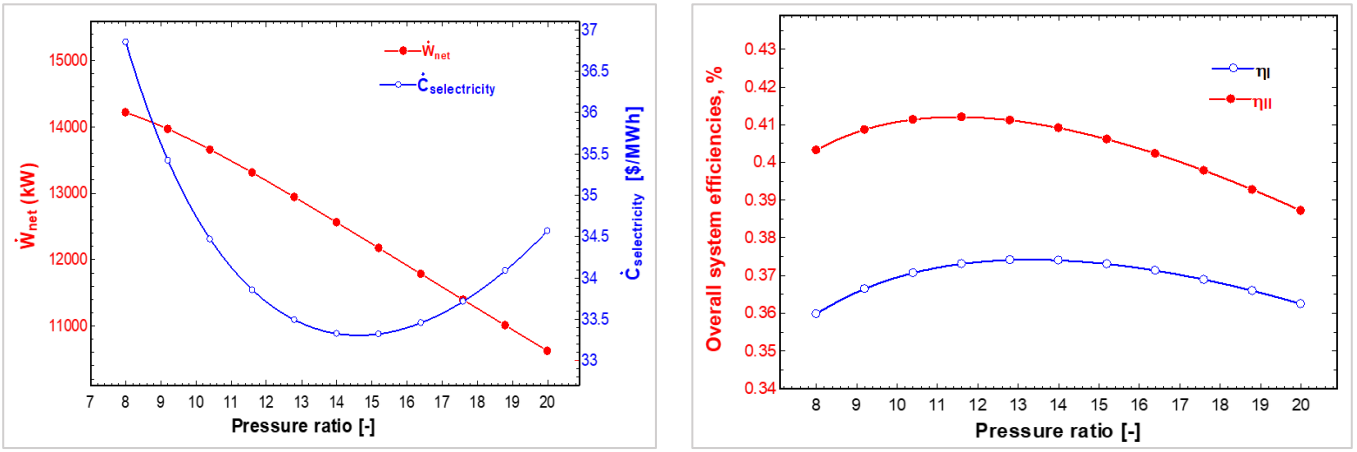

(a) **(b)**

Figure 6: Variation of work, a) electricity cost rate, and b) overall efficiencies of the system according to the pressure ratio

Figures 7a and 7b illustrate the effect of gas turbine inlet temperature (T_4) on the power output, electricity cost rate, and system efficiencies within the solar-based triple combined cycle system. This analysis highlights GTIT as a crucial design and optimization parameter for enhancing the performance of solar-based triple combined cycle (TCC) systems. Raising the gas turbine inlet temperature significantly enhances the network output, thermal efficiency, and exergy efficiency, as well as the cost-effectiveness of electricity generation. Figure 7a illustrates that increasing GTIT leads to higher power output and lower cost per unit of electricity, enhancing both economic and energetic performance. Net Work Output Increases linearly with GTIT, rising from ~6,000 kW at 800 °C to ~14,000 kW at 1050 °C. This reflects improved gas turbine performance and greater thermal energy conversion at higher inlet temperatures. The electricity cost rate decreases steadily from ~38 $/MWh at 800 °C to ~32.5 $/MWh at 1050 °C. The inverse relationship suggests that higher thermal efficiency results in lower operational costs. Figure 7b shows that both efficiencies improve with GTIT, confirming that higher turbine inlet temperatures support more efficient and effective energy use. First-Law Efficiency rises from ~28% to ~37% as GTIT increases. Shows improved energy conversion efficiency due to enhanced turbine work. Exergy Efficiency also increases, from ~32% to ~44.5%, reflecting better utilization of available energy considering irreversibilities. Always higher than first-law efficiency, indicating superior performance when accounting for exergy analysis.

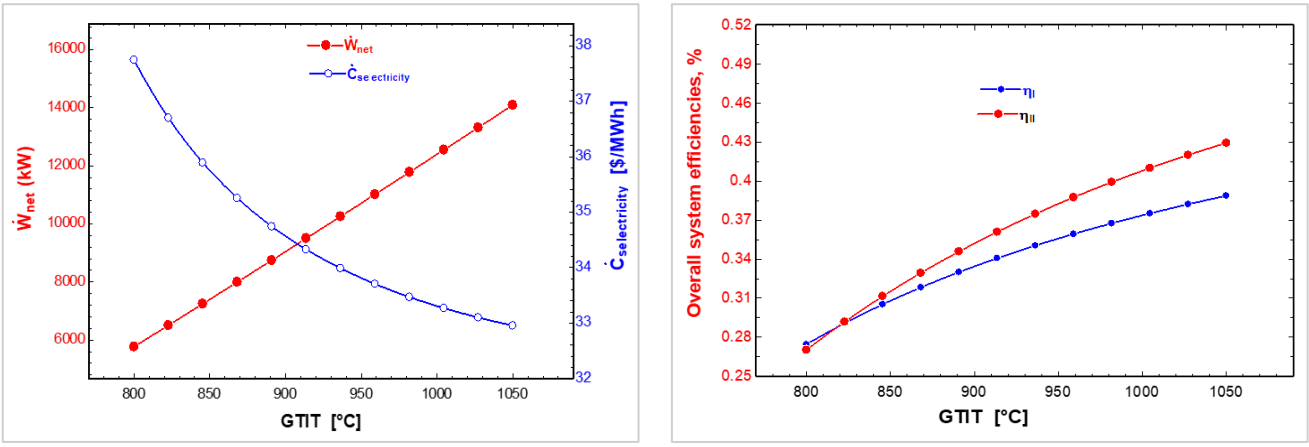

(a) **(b)**

Figure 7: Variation of work, a) electricity cost rate, and b) overall system efficiencies according to the gas turbine inlet temperature

Figure 8 illustrates the monthly variation in energy source contributions, solar and fuel, as a percentage of total heat input in the solar-based triple combined cycle system. The figure effectively captures the seasonal shift in dependency between renewable and conventional energy sources. These results confirm the dynamic interplay between solar and fuel sources in a hybrid power system. It reveals both the strengths of solar energy in reducing fuel use during high-radiation months and the challenges of maintaining performance during periods of low solar activity. The chart clearly reflects the impact of solar irradiance availability on the system's energy source mix. High solar shares in summer reduce fuel consumption. Increased fuel dependency in winter results from lower solar radiation, underscoring the system's need for support mechanisms such as efficient thermal energy storage (TES), adaptive hybrid control strategies, and seasonal operation planning to maximize renewable energy use. June is the most solar-reliant month, with over 80% of the system's energy input coming from solar sources. December marks the lowest

solar share (~40%) and the highest reliance on fuel. The seasonal transition is gradual, with solar use increasing from March to June, then decreasing after August. Solar energy dominates in Summer Months (May–August), reaching peak contribution levels in June (~82%) while in July and May it go to (~75–80%). The fuel share is at its lowest during this period, specifically in June (~18%) and July (~22%). Fuel becomes the primary source of heat input during the winter months (January–March and November–December). Fuel share exceeds 60% in December and January, and solar contributions drop to ~40% or below. The transitional months (April, September, October show more balanced contributions, with each source accounting for roughly 50% of the heat input.

Figure 9 illustrates the monthly variation in the net power output of the solar-based triple combined cycle system, measured in kilowatts (kW). It captures how the system's electrical performance changes throughout the year. The figure reveals that Winter months are more favorable for high energy output due to improved thermodynamic efficiency and higher fuel use. The summer months typically exhibit a performance dip, largely attributed to thermal efficiency losses resulting from elevated temperatures and the lower energy density of solar heat. To optimize year-round performance, the system would benefit from advanced cooling strategies during the summer and improved solar collection and heat transfer systems to enhance energy quality, as well as hybrid control systems that adaptively balance solar and fuel sources to stabilize power output. Higher outputs in winter (January and December) are due to Lower ambient temperatures, which enhance gas turbine efficiency by improving air compression, and a greater use of fuel, which generally produces higher-quality thermal energy compared to solar energy. Lower outputs in summer (June–August) are due to high ambient temperatures, which reduce compressor efficiency and turbine performance, as well as an increased reliance on solar energy, which, although renewable, typically results in lower thermal energy density compared to fossil fuels. The findings also present that January and December both show the maximum net power output, each reaching approximately 14,200 kW. November follows closely with slightly lower values. July records the lowest output, around 12,500 kW. June and August are also among the months with reduced output, indicating a mid-year dip. Spring months, such as March, April, and May, exhibit stable and moderately high output, ranging from 13,000 to 13,800 kW. A gradual increase is seen starting in September, recovering towards the winter peak.

Figure 10 displays the monthly variation in the electricity cost rate of the solar-based triple combined cycle system, measured in dollars per megawatt-hour ($/MWh). It reflects how energy generation costs fluctuate across different months of the year. The results showed that lower electricity costs in summer directly correlate with increased solar energy usage, which eliminates fuel expenses. Higher costs in winter are driven by increased fuel consumption, which is necessary to compensate for reduced solar irradiance. The system experiences economic peaks and troughs in line with solar availability patterns. The maximum cost rate was obtained in December (~$52/MWh), while the minimum cost rate was obtained in June (~$33/MWh). The cost difference between peak and trough is ~19$/MWh. The winter months (January–March, November–December) exhibit the highest electricity cost rates, with January and December peaking at around $ 50–52/MWh. November and February follow closely, with values just below $50 per MWh. The summer months (May–August) typically exhibit the lowest electricity costs, with June being the lowest, at approximately 33$/MWh. May, July, and August also maintain relatively low-cost rates, ranging from $34 to $ 37/MWh. Cost rates in the transitional months (April, September, October) are moderate, rising from the summer low toward the winter high. October shows a notable increase (~$45/MWh), marking the seasonal transition to fuel-reliant months.

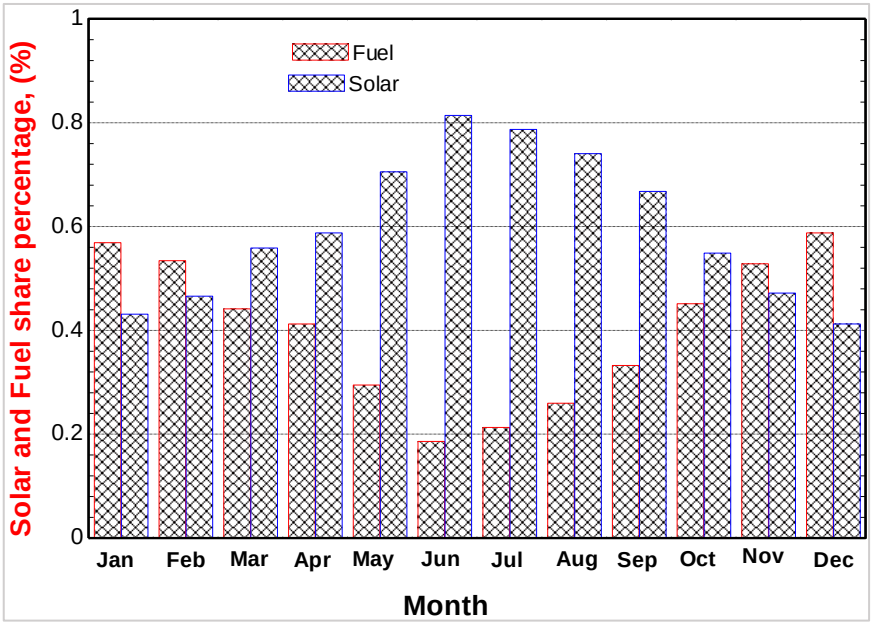

Figure 8: Variation of solar and fuel shares below each month

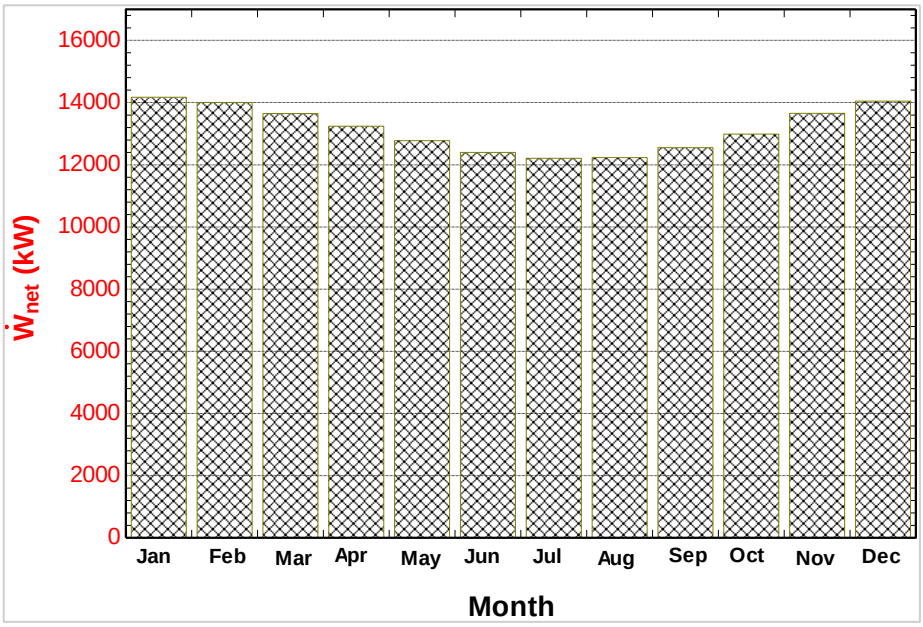

Figure 9: Variation of the system's work net for each month

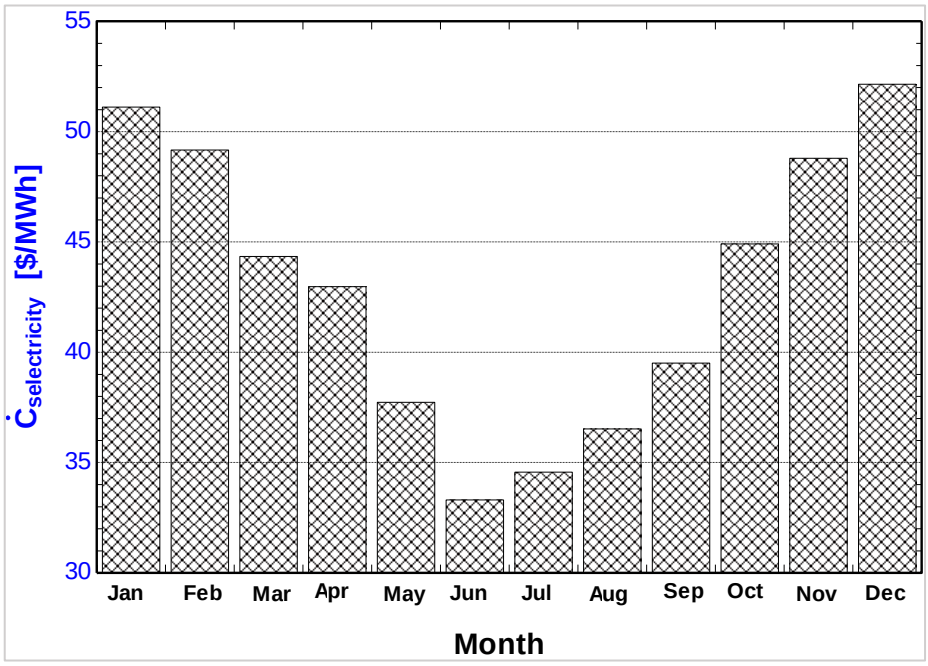

Figure 10: Variation in the system's electricity cost rate per month

Figure 11 presents the monthly variation of CO_2 emissions (kg/kWh) from the solar-based triple combined cycle system over the year. The findings indicate that lower emissions in summer are associated with increased solar energy utilization, which replaces fossil fuel usage and reduces carbon output. Higher emissions in winter are attributed to increased fuel consumption resulting from low solar irradiance, which necessitates the use of backup fuels. The pattern mirrors seasonal solar availability, further supporting the effectiveness of solar integration in reducing environmental impact. The maximum CO_2 emissions were obtained in December (~0.33 kg/kWh), while the minimum CO_2 emissions were obtained in June (~0.10 kg/kWh). The data indicate a strong inverse correlation between the share of solar energy and CO_2 emissions. The winter months (January–March, November–December) exhibit higher CO_2 emissions, with values ranging from 0.30 to 0.33 kg/kWh in January and December. The peak occurs in December, reaching approximately 0.33 kg/kWh, the highest value of the year. The lowest CO_2 emissions are recorded in summer Months (May–August), especially in June, with a minimum value of around 0.10 kg/kWh. May and July also show relatively low emissions (~0.12–0.15 kg/kWh). Emissions in these transitional months (April, September, and October) are moderate, ranging from 0.20 to 0.25 kg/kWh. A gradual rise begins from September, indicating the return of fuel dependency.

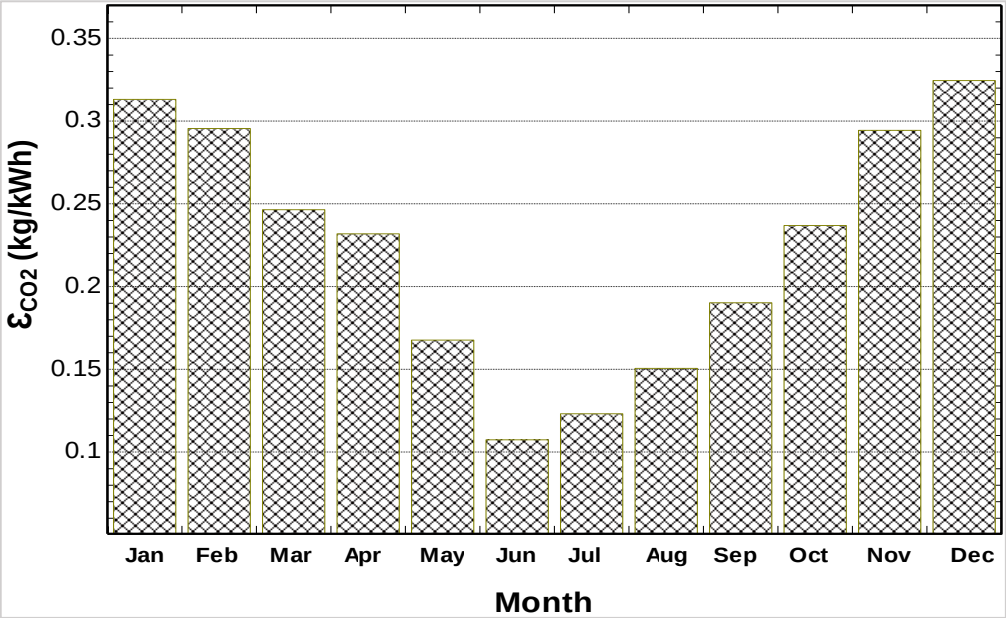

Figure 11: Variation of the CO_2 mission under each month

6. Conclusion

This study explored an innovative solar-powered electricity generation system utilizing a TCC, focusing on thermodynamic (energy and exergy) and exergoeconomic analyses. The system is powered by concentrated solar power (CSP) collected in Tikrit, Iraq, integrating rock bed energy storage (RBES) with three power cycles: a gas turbine cycle, a steam Rankine cycle, and an organic Rankine cycle. The RBES stores thermal energy from the gas turbine exhaust for 10 hours, which is then utilized to operate the steam cycle for an additional 14 hours, ensuring continuous electricity generation. The study examined how key operational parameters, including ambient temperature, pressure ratios, and component efficiencies, impact system performance and electricity production costs. The results led to several significant conclusions:

1) The system's highest power output of 14,172 kW occurs in January, while the lowest output of 12,207 kW is recorded in July, primarily due to seasonal variations in solar energy availability and thermal efficiency.
2) Electricity cost is lower in summer and higher in winter, as solar energy contributes more in summer, reducing fuel dependency. The electricity cost rate is $33.31 per MWh in June but rises to $52.14 per MWh in December due to increased fuel consumption.
3) The system's exergo-economic factor (f_k) reaches an impressive 64.58%, demonstrating strong economic feasibility, which could encourage government investment in deploying this technology in Iraq.
4) Exergy destruction cost analysis reveals a total system cost of $140.7 per hour, with the combustion chamber incurring the highest exergy destruction cost at $55.07 per hour, while the pump incurs the lowest cost at just $ 0.10 per hour.
5) Ambient temperature has a significant impact on system performance and electricity costs, underscoring the importance of considering local climate conditions during the design phase.
6) Increasing the gas turbine inlet temperature (T_4) significantly enhances system performance and efficiency, while reducing electricity costs; therefore, higher T_4 values are a key optimization parameter for maximizing system effectiveness.

These findings offer valuable insights into optimizing solar-based power generation, highlighting the importance of thermal energy storage, operational efficiency, and economic viability in developing sustainable energy solutions for regions with high solar potential, such as Iraq.

Author contributions

Conceptualization, **A. Akroot,** and **A. Faraj**; data curation, **A. Akroot**; formal analysis, **A. Faraj**; investigation, **A. Akroot,** and **A. Faraj**; methodology, **A. Akroot**; project administration, **A. Faraj**, resources, **A. Faraj**; software, **A. Akroot**; supervision, **A. Akroot**; validation, **A. Akroot,** and **A. Faraj**; visualization, **A. Akroot**; writing—original draft preparation, **A. Faraj**; writing—review and editing, **A. Akroot**. All authors have read and agreed to the published version of the manuscript.

Funding

This research received no specific grant from any funding agency in the public, commercial, or not-for-profit sectors.

Data availability statement

The data that support the findings of this study are available on request from the corresponding author.

Conflicts of interest

The authors declare that there is no conflict of interest.,

References

[1] Z. Ma, G. C. Glatzmaier, C. F. Kutscher, Thermal energy storage and its potential applications in solar thermal power plants and electricity storage, ASME 2011 5th International Conference on Energy Sustainability, 2011, 447-456. https://doi.org/10.1115/ES2011-54077

[2] W. Strielkowski, L. Civin, E. Tarkhanova, M. Tvaronavi, Y. Petrenko, Renewable Energy in the Sustainable Development of Electrical, Energies, 14 (2021) 1-24. https://doi.org/https://doi.org/10.3390/en14248240

[3] H. M. Delibas, E. Kayabasi, Energy, Environment And Economy Assessment Of Waste Heat Recovery Technologies In Marine Industry, Mater. Eng. Technol., 2 (2019) 39-45.

[4] S. Kuravi, J. Trahan, D. Y. Goswami, M. M. Rahman, E. K. Stefanakos, Thermal energy storage technologies and systems for concentrating solar power plants, Prog. Energy. Combust. Sci., 39 (2013) 285-319. https://doi.org/10.1016/j.pecs.2013.02.001

[5] F. Marongiu, S. Soprani, K. Engelbrecht, et. al, Modeling of high temperature thermal energy storage in rock beds – Experimental comparison and parametric study, Appl. Therm. Eng., 163 (2019) 114355. https://doi.org/10.1016/j.applthermaleng.2019.114355

[6] S. Soprani, F. Marongiu, L. Christensen, O. Alm, K. Dinesen, T. Ulrich, K. Engelbrecht, Design and testing of a horizontal rock bed for high temperature thermal energy storage, Appl. Energy, 251 (2019) 113345. https://doi.org/10.1016/j.apenergy.2019.113345

[7] Y. Muhammad, P. Saini, K. Knobloch, H. L. Frandsen, K. Engelbrecht, Rock bed thermal energy storage coupled with solar thermal collectors in an industrial application : Simulation , experimental and parametric analysis, J. Energy Storage, 67 (2023) 107349. https://doi.org/10.1016/j.est.2023.107349

[8] N. B. Desai, M. E. Mondejar, F. Haglind, Techno-economic analysis of two-tank and packed-bed rock thermal energy storages for foil-based concentrating solar collector driven cogeneration plants, Renew. Energy, 186 (2022) 814-830. https://doi.org/10.1016/j.renene.2022.01.043

[9] G. Zanganeh, A. Pedretti, S. Zavattoni, M. Barbato, A. Steinfeld, Packed-bed thermal storage for concentrated solar power - Pilot-scale demonstration and industrial-scale design, Solar Energy, 86 (2012) 3084-3098. https://doi.org/10.1016/j.solener.2012.07.019

[10] I. Ortega-Fernández, I. Uriz, A. Ortuondo, A. B. Hernández, A. Faik, I. Loroño, J. Aseguinolaza, Operation strategies guideline for packed bed thermal energy storage systems, Int. J. Energy Res., 43 (2019) 6211-6221. https://doi.org/10.1002/er.4291

[11] T. Nahhas, X. Py, N. Sadiki, Experimental investigation of basalt rocks as storage material for high- temperature concentrated solar power plants, Renewable Sustainable Energy Rev., 110 (2019) 226-235. https://doi.org/10.1016/j.rser.2019.04.060

[12] M. Ozturk, I. Dincer, N. Javani, Thermodynamic modeling of a solar energy based combined cycle with rock bed heat storage system, Solar Energy, 200 (2020) 51-60. https://doi.org/10.1016/j.solener.2019.03.053

[13] L. Heller, P. Gauché, Modeling of the rock bed thermal energy storage system of a combined cycle solar thermal power plant in South Africa, Solar Energy, 93 (2013) 345-356. https://doi.org/10.1016/j.solener.2013.04.018

[14] A. Sharma, P. K. Pandey, M. Didwania, Techno-economic optimization of packed-bed thermal energy storage system combined with CSP plant using DOE: design of experiment technique and Taguchi method, Int. J. Energy Environ. Eng., 14 (2022) 287-308. https://doi.org/10.1007/s40095-022-00526-0

[15] A. Abdulla, K. S. Reddy, Effect of operating parameters on thermal performance of molten salt packed-bed thermocline thermal energy storage system for concentrating solar power plants, Int. J. Therm. Sci., 121 (2017) 30-44. https://doi.org/10.1016/j.ijthermalsci.2017.07.004

[16] B. Kocak, H. Paksoy, Performance of laboratory scale packed-bed thermal energy storage using new demolition waste based sensible heat materials for industrial solar applications, Solar Energy, 211 (2020) 1335-1346. https://doi.org/10.1016/j.solener.2020.10.070

[17] Çengel Y. A., and Boles M. A., Thermodynamics: An Engineering Approach, 5th ed. New York: McGraw-Hill, 2006.

[18] Moran, M. J., Shapiro, H. N. , Boettner, D. D., Bailey, M. B., Fundamentals of Engineering Thermodynamics; John Wiley & Sons, 2010.

[19] Z. Aghaziarati, A. H. Aghdam, Thermoeconomic analysis of a novel combined cooling, heating and power system based on solar organic Rankine cycle and cascade refrigeration cycle, Renew. Energy, 164 (2021) 1267-1283. https://doi.org/10.1016/j.renene.2020.10.106

[20] A. Tozlu, E. Kayabasi, H. Ozcan, Thermoeconomic analysis of a low-temperature waste-energy assisted power and hydrogen plant at off-NG grid region, Sustain. Energy Technol. Assess., 52 (2022) 102104. https://doi.org/10.1016/j.seta.2022.102104

[21] M. Ozturk, I. Dincer, N. Javani, Thermodynamic modeling of a solar energy based combined cycle with rock bed heat storage system, Solar Energy, 200 (2020) 51-60. https://doi.org/10.1016/j.solener.2019.03.053

[22] W. Talal, A. Akroot, Exergoeconomic Analysis of an Integrated Solar Combined Cycle in the Al-Qayara Power Plant in Iraq, Processes, 11 (2023) 656. https://doi.org/10.3390/pr11030656

[23] M. E. Demir, I. Dincer, Development of a hybrid solar thermal system with TEG and PEM electrolyzer for hydrogen and power production, Int. J. Hydrog. Energy, 42 (2017) 30044-30056. https://doi.org/10.1016/j.ijhydene.2017.09.001

[24] S. Barakat, A. Ramzy, A. M. Hamed, S. H. El Emam, Enhancement of gas turbine power output using earth to air heat exchanger (EAHE) cooling system, Energy Convers. Manag., 111 (2016) 137-146. https://doi.org/10.1016/j.enconman.2015.12.060

[25] K. Abudu, U. Igie, I. Roumeliotis, R. Hamilton, Impact of gas turbine flexibility improvements on combined cycle gas turbine performance, Appl. Therm. Eng., 189 (2021) 116703. https://doi.org/10.1016/J.APPLTHERMALENG.2021.116703

[26] A. Akroot, A. Nadeesh, Performance Analysis of Hybrid Solid Oxide Fuel Cell-Gas Turbine Power System, Int. J. Eng. Sci., 9 (2020) 43-51 . https://doi.org/10.9790/1813-0909014351

[27] A. Akroot, L. Namli, Performance assessment of an electrolyte-supported and anode-supported planar solid oxide fuel cells hybrid system, J. Ther. Eng., 7 (2021) 1921-1935. https://doi.org/10.14744/jten.2021.0006

[28] A. Akroot, Effect of Operating Temperatures on the Performance of a SOFCGT Hybrid System, In. J. of Trend in Sci. Res. and Development, 3 (2019) 1512-1515. https://doi.org/10.31142/ijtsrd23412

[29] A. Akroot, L. Namli, H. Ozcan, Compared Thermal Modeling of Anode- and Electrolyte-Supported SOFC-Gas Turbine Hybrid Systems, J. Electrochem. Energy Convers. Storage, 18 (2021) 011001. https://doi.org/10.1115/1.4046185

[30] K. Seshadri, Thermal design and optimization: A. Bejan, G. Tsatsaronis, and M. Moran, Wiley Interscience, John Wiley Sons Inc., New York (1996), Energy, 21 (1996) 433-434. https://doi.org/10.1016/s0360-5442(96)90000-6

[31] L. Elmorsy, T. Morosuk, G. Tsatsaronis, Exergy-based analysis and optimization of an integrated solar combined-cycle power plant, Entropy, 22 (2020) 1-20. https://doi.org/10.3390/e22060655

[32] H. Ozcan, E. Kayabasi, Thermodynamic and economic analysis of a synthetic fuel production plant via CO2 hydrogenation using waste heat from an iron-steel facility, Energy Convers. Manag., 236 (2021) 114074. https://doi.org/10.1016/j.enconman.2021.114074

[33] F. Mohammadkhani, N. Shokati, S. Mahmoudi, M. Yari, M. Rosen, Exergoeconomic assessment and parametric study of a Gas Turbine-Modular Helium Reactor combined with two Organic Rankine Cycles, Energy, 65 (2014) 533-543. https://doi.org/10.1016/J.ENERGY.2013.11.002

[34] M. Nourpour, M. H. Khoshgoftar Manesh, Evaluation of novel integrated combined cycle based on gas turbine-SOFC-geothermal-steam and organic Rankine cycles for gas turbo compressor station, Energy Convers. Manag., 525 (2022) 115050. https://doi.org/10.1016/j.enconman.2021.115050

[35] A. F. Kareem, A. Akroot, H. A. Wahhab, W. Talal, R. M. Ghazal, Exergo-Economic and Parametric Analysis of Waste Heat Recovery from Taji Gas Turbines Power Plant Using Rankine Cycle and Organic Rankine Cycle, 15 (2023) 9376. http://dx.doi.org/10.3390/su15129376

[36] A. Lazzaretto, G.Tsatsaronis, SPECO: A systematic and general methodology for calculating efficiencies and costs in thermal systems, Energy, 31 (2006) 1257-1289. https://doi.org/10.1016/j.energy.2005.03.011

[37] A. M. Elsafi, Exergy and exergoeconomic analysis of sustainable direct steam generation solar power plants, Energy Convers. Manag., 103 (2015) 338-347. https://doi.org/10.1016/j.enconman.2015.06.066